Military Technical College
Kobry Elkobbah,
Cairo, Egypt

8th International Conference on
Aerospace Sciences &
Aviation Technology

ON THE PENETRATION OF HIGH-SPEED LONG RODS INTO THICK STEEL TARGETS

A. M. RIAD*

ABSTRACT

In this paper, the modified form of Jones et al. model introduced by Moustafa et al. [1], Model I, describing the penetration of a thick metallic target by a continuous rod is examined for the following conditions: (i) the rod impact velocity is greater than 1.5 km/s and (ii) the rod aspect ratio is greater than 10. The predicted depths of penetration are compared with experimental measurements of Buchar et al. [2]. Model I proves its limited predictive capabilities; it can be only applied to describe the penetration of a long rod into a thick metallic target at impact velocities less than 1.6 km/s.

Moreover, the hydrodynamic theory developed by Tate [3,4] is modified herein by considering the essential dependence of target strength factor on the rate of its material deformation. Three different forms are used to determine the target strength factor; one is linear, whereas the other two forms are non-linear. The linear form correlates the target strength factor with rod impact velocity. The first non-linear form correlates this factor with rod impact velocity, whereas the second correlates it with rod impact velocity and aspect ratio. The modified Tate model, Model II, is used to cover the deficiencies of Model I. The predicted depths of penetration of Model II are compared with experimental measurements of Buchar et al. [2]; good agreement is generally obtained when the linear form that determines the target strength factor is used. Model II is also used to predict samples of time histories of penetration depth and rod residual length due to the impact of high-speed long steel rods of different strengths into thick steel targets. In addition, the model is used to study the influence of rod strength and impact velocity, respectively, on the depth of penetration and the rod residual length.

KEY WORDS

- High-Speed Impact
- Solid Mechanics
- Thick Steel Targets
- Penetration Mechanics
- Long-Rod Penetrators

---

* Lecturer, Chair of Weapons and Ammunition, M.T.C., Cairo, Egypt.

INTRODUCTION

In the last three decades, the penetration of a high-speed long rod into a thick metallic target has become one of the basic research topics in terminal ballistics. The modified hydrodynamic penetration theory developed by Tate [3,4] has been widely used as a simple tool for describing this event. The model accounts for the penetration depth and the rod deceleration as a function of rod's impact velocity. The theory is based on a modified Bernoulli equation which equates the pressure on both sides of the moving rod-target interface. This equation includes two strength factors for the rod and target, respectively, which are determined empirically. Tate recommended the Hugoniot Elastic limit (HEL) of the rod material as its strength factor and a value of 3.5*(HEL) of the target material as its strength factor. Experimental results of Hohler and Stilp [5] support Tate's suggestion.

Jones et al. [6] modified the one-dimensional hydrodynamic theory developed by Tate [3,4]. They modified the equation of motion of the rod rigid part to account for the mass transferring into plastic region. Moreover, the mushroom strain at the deformed end of the rod is incorporated into their analysis. They used the ultimate strengths of both rod and target materials, respectively, to represent their strength factors. Wilson et al. [7] modified Jones et al. model by considering the effect of engineering strain at the penetrator tip on its erosion rate.

The hydrodynamic theory developed by Tate was examined by Rosenberg et al. [8]. They applied the modified Bernoulli equation to the forces acting on both sides of the moving rod-target interface. Moreover, they assumed the effective cross-sectional area of the mushroomed end of the rod to be at least twice the value of its rigid part. They derived an analytical expression to account for the target strength factor and found it to be 3 : 4 times the compressive yield strength of the target material. Their predicted results give good agreement with experimental measurements over a narrow range of impact velocity (1408 up to 1505 m/s).

Moustafa et al. [1] derived the main equations comprising Jones et al. model [6] considering the effect of engineering strain at the penetrator tip on its erosion rate, as introduced by Wilson et al. [7]. Moreover, they modified this model by accounting for the dependence of target strength factor on the rate of material deformation; they considered this factor to vary linearly with impact velocity. They compared the predicted results of their model with the experimental measurements of Wilson et al. [7], which were essentially limited to rod aspect ratios $L/D \leq 10$. Poor agreement between predicted depths of penetration and experimental measurements was obtained when rod impact velocity exceeded 2 km/s.

In the following, the model modified by Moustafa et al. [1] is examined by comparing its predicted depths of penetration with experimental measurements of Buchar et al. [2]. Moreover, the one-dimensional hydrodynamic theory developed

by Tate [3,4] is modified by accounting for the dependence of target strength factor on the rate of deformation of its material. Three forms determining the target strength factor are introduced; one is linear, whereas the other two forms are non-linear. The linear form correlates the target strength factor with rod impact velocity. The first non-linear form correlates the target strength factor with impact velocity, whereas the second correlates this factor with rod impact velocity and aspect ratio. The predicted depths of penetration of the modified Tate model are compared with the experimental measurements of Buchar et al. [2]. Samples of predicted time histories of penetration depth and rod residual length using the modified Tate model are presented. In addition, the effects of rod strength and impact velocity, respectively, on the rod penetration depth and residual length are discussed.

MAIN EQUATIONS OF MODELS CONSIDERED

Jones et al. model modified by Moustafa et al. [1] and the modified Tate model, hereinafter termed Models I and II, describe the penetration of a thick metallic target by a high-speed long rod. Both models are divided into a main phase and two complementary phases. These are: (i) hydrodynamic penetration, (ii) rigid-rod penetration and (iii) no-penetration phases, respectively. Therefore, the penetration process could be considered to consist of phase (i) or a combination of phase (i) and one of the other two phases. The sequence of the penetration phases that represent the complete penetration process depends on the relative magnitudes of the rod and target strength factors as well as the impact velocity of the rod.

The main equations representing each penetration phase are listed in Table 1 for both models. For each phase, the main equations represent a system of first order dependent differential equations. The time of penetration is considered as the independent variable. Each system is solved numerically; the end conditions of the current phase represent the initial conditions for the subsequent phase.

RESULTS AND DISCUSSIONS

(i) Evaluation of Analytical Models

In the following, the experimental measurements obtained by Buchar et al. [2] are used to evaluate the analytical models considered herein. These measurements pertain to impact of high strength steel rods of different mechanical properties into thick steel targets. The chemical composition (in wt. %) of the steel used for rod and target is: 0.75 C, 1.8 Mn, 1.68 Si, 0.08 Cu, 0.014 P, 0.005 S, 1.03 Cr, and 0.14 Ni. Buchar et al. changed the mechanical properties of the steel rods by subjecting them to different heat treatments. The tensile mechanical properties

Table 1. Main equations representing each penetration phase of both models.

Model I	Model II
I- Hydrodynamic penetration Phase ($R_t > Y_p$ or $Y_p > R_t$):	
* Modified Bernoulli equation (equating interface pressure):	
$$P = R_t + 1/2\ \rho_t U^2 = Y_p + 1/2\ \rho_p (V-U)^2, \quad (1)$$	
R_t : target strength factor, Y_p : rod strength factor, P: interface pressure, ρ_t : density of target material, U: penetration velocity, ρ_p : density of rod material, V: velocity of rod rigid part.	
* Rod and target strength factors:	
$$Y_p = 1.7\ \sigma_{yp}^{D}, \quad (2)a$$	
$$R_t = C_t\ \sigma_{yt}^{D}, \quad (2)b$$	
$$C_t = a + b\ V_i, \quad (2)c$$	$$C_t = a\ V_i + b\ V_i^2 \quad (2)d$$
	$$= a + b\ V_i + c\ \ln (L/D). \quad (2)e$$
σ_{yp}^{D} : dynamic yield strength of rod material, C_t : target strength multiplier, σ_{yt}^{D} : dynamic yield strength of target material, a, b, and c: coefficients, L: initial length of rod, D: initial diameter of rod.	
* Equation of motion of rod rigid part:	
$$dV/dt = -[(Y_p/\rho_p)+(V-U)^2\ (1.5e+1)/e]/\ (l\ (1+e)), \quad (3)$$	$$dV/dt = -\ Y_p\ /(\rho_p\ l), \quad (3)^{*}$$
e: compressive engineering strain at the tip of the rod, l : current length of rod rigid part.	
* Decreasing rate of length of rod rigid part:	
$$dl/dt = (V-U)/e. \quad (4)$$	$$dl/dt = -\ (V-U). \quad (4)^{*}$$
* Rate of change of rod penetration depth Z with time:	
$$dZ/dt = U. \quad (5)$$	
* End conditions:	
$$R_t > Y_p,\ U = 0.0 \text{ and } V = (2(R_t - Y_p)/\ \rho_p)^{0.5}. \quad (6)a$$	
$$Y_p > R_t,\ U = V \text{ and } V = (2(Y_p\ -R_t\ )/\ \rho_t)^{0.5}\ . \quad (6)b$$	
II- Rigid-rod penetration phase ($Y_p > R_t$):	
* Interface pressure P:	
$$P = R_t + 1/2\ \rho_t U^2 = Y_p. \quad (7)$$	
* Equation of motion of the rod:	
$$dV/dt = -[\ R_t + 1/2\ \rho_t V^2\ ]/(l_r\ \rho_p\ (1+e)), \quad (8)$$	$$dV/dt = -\ Y_p\ /(\rho_p\ l_r), \quad (8)^{*}$$
l_r : length of rod rigid part at the end of hydrodynamic penetration phase.	

Table 1. Main equations representing each penetration phase of both models. (Continued).

Model I	Model II
* Rate of change of rod penetration depth Z with time: $dZ/dt = U.$ (9)	
* End condition: $U = V = 0.0.$ (10)	
III- <u>No-penetration phase ($R_t > Y_p$)</u>: * Interface pressure P: $P = Y_p + 1/2\ \rho_p V^2 = R_t.$ (11)	
* Equation of motion of rod rigid part (impact into rigid surface): $dV/dt=-[(Y_p/\rho_p)+V^2(1.5e+1)/e] / (l(1+e)).$ (12)	$dV/dt = - Y_p /(\rho_p l).$ (12)*
* Decreasing rate of length of rod rigid part: $dl/dt = V/e.$ (13)	$dl/dt = - V.$ (13)*
* End condition: $V = 0.0.$ (14)	

of the steel rods and target are listed in Table 2. The rods were fired at normal incidence against the targets with impact velocities ranging from 1400 up to 2400 m/s.

Buchar et al. [2] introduced six groups of experimental data. Three parameters are found to vary in these data; these are rod strength, impact velocity and rod aspect ratio (L/D). For each group, the dimensions and densities of the rod and target materials are listed in Table 3. The hard and soft steel rods were designated by S-H and S-S, respectively, whereas the target is designated by S-T. A number representing the rod aspect ratio is added to each rod designation.

(a) Predicted penetration depth using Model I

In order to run the computer program of Model I, it is necessary to determine the value of target strength factor. This factor was correlated with the dynamic yield strength of target material through a multiplier; this multiplier is considered to vary linearly with impact velocity (cf. Eqns. (2)b and (2)c). Therefore, the values of the coefficients, a and b, of the multiplier equation should be determined. The measured depths of penetration by Buchar et al. [2] were used to determine the values of target strength multiplier. Table 4 lists the values of the coefficients due to the different interactions of rod and target materials. Moreover, Figs 1 up to 4 depict the predicted multiplier values that match the experimental measurements of penetration depth with the predicted values as a function of impact velocity for

Table 2. Main quasi-static properties of rods and target materials [2].

Object	Yield strength [MPa]	Ultimate strength [MPa]	Hardness [HB]
Rod (hard)	1476	1941	514
Rod (soft)	930	970	293
Target	840	900	269

Table 3. Main dimensions, densities and designations of rod and target materials.

Group No.	Rod					Target	
	Mat. Desig.	L [mm]	D [mm]	L/D	ρ_p [kg/m^3]	Mat. Desig.	ρ_t [kg/m^3]
1	S-S-12	252	21	12	7810	S-T	7810
2	S-H-12	252		12			
3	S-S-18	378		18			
4	S-H-18	378		18			
5	S-S-25	525		25			
6	S-H-25	525		25			

Table 4. Values of coefficients of Eqn. (2)c.

Group No.	Material Designation		Equation (2) c			
			Model I		Model II	
	Rod	Target	a	b (s/m)	a	b (s/m)
1	S-S-12	S-T	1.534E+1	-7.916E-3	7.821	-2.358E-3
2	S-H-12		4.753	-2.018E-3	5.8	-1.169E-3
3	S-S-18		1.486E+1	-7.151E-3	6.629	-1.24E-3
4	S-H-18		1.533E+1	-7.423E-3	6.445	-9.801E-4
5	S-S-25		1.236E+1	-4.83E-3	5.216	1.344E-4
6	S-H-25		1.06E+1	-3.828E-3	3.773	1.021E-3

four rod-target interactions. The straight line fits that correlate the multiplier with impact velocity are also depicted on their respective figures.

For each group, it is clear from the aforementioned figures that the multiplier is a decreasing function of impact velocity. For soft and hard steel rods having an aspect ratio of 12, the multiplier is always greater than unity for impact velocities less than 1800 m/s. For higher impact velocities, the multiplier is taken equal to unity, which means that the target strength factor attains its lowest possible

value, i.e. dynamic yield strength. The impact velocity at which the multiplier decreases to unity is less than 1900 m/s for rods having an aspect ratio of 18, whereas the multiplier is greater than unity for rods having an aspect ratio of 25 over the whole range of impact velocity (cf. Figs. 3,4).

For each group of experimental results, the straight line equation that correlates the multiplier with impact velocity was fed into the computer program. The program was run to predict the depth of penetration at each impact velocity. For each group, Table 5 lists the depth of penetration measured by Buchar et al. [2], the predicted depth of penetration using Model I and the corresponding values of the multiplier.

Figures 5 up to 8 depict the change of depth of penetration with impact velocity for four rod-target interactions as predicted by Model I. In addition, the experimental measurements of Buchar et al. [2] are depicted on their respective figures. It is clear from these figures that the predicted depths of penetration are in good agreement with experimental measurements up to V_i = 1700 m/s for soft steel rods having an aspect ratio of 12, V_i = 1550 m/s for hard steel rods having the same aspect ratio and V_i = 1900 m/s for rods having an aspect ratio of 18. For higher impact velocities, poor agreement is generally obtained. For rods having an aspect ratio of 25, good agreement between predicted depths of penetration and experimental measurements is generally obtained (see Table 5).

From the aforementioned predicted results, it is clear that Model I has generally limited predictive capabilities when the impact velocity of the rod is greater than 1600 m/s. Therefore, Model I can be only applied to describe the penetration of a long rod (L/D $\geq$ 10) into a thick steel target when the impact velocity of the rod is less than 1600 m/s.

(b) Predicted penetration depth using Model II

Values of the coefficients of the linear relation that correlates the target strength multiplier with impact velocity (cf. Eqn. (2)c) are determined by matching the measured depths of penetration of Buchar et al. [2] with predicted values obtained by Model II. Table 4 lists the values of these coefficients, whereas Figs. 1 up to 4 also depict the predicted multipliers as a function of impact velocity for four rod-target interactions that were examined by Model I. The straight line fits that correlate the multiplier with impact velocity are also depicted on their respective figures.

It is clear that the multiplier is a decreasing function of impact velocity for rods having the aspect ratios of 12 and 18. However, the multiplier is always greater than unity over the used range of impact velocity. For rods having an aspect ratio of 25, the multiplier is an increasing function of impact velocity. For each group of experimental data, the straight line fit that correlates the multiplier with impact velocity was fed into the program. The program predicted the depth of penetration

Table 5. Comparison between the experimental measurements of Buchar et al. [2] and predicted results of both models.

Group No.	Material designation		Impact velocity V_i [m/s]	Measured depth [2] Z [mm]	Model I		Model II			
	Rod	Target			Multiplier of Eqn. (2) c, C_t	Depth using Eqn. (2) c, Z [mm]	Multiplier of Eqn. (2) c, C_t	Depth using Eqn. (2) c, Z [mm]	Depth using Eqn. (2) d, Z [mm]	Depth using Eqn. (2) e, Z [mm]
1	S-S-12	S-T	1526	99	3.3	99.8	4.33	103.22	109.85	103.26
			1546	104	3.1	104.15	4.28	107.95	113.48	107.99
			1637	125	2.3	123.35	4.06	128.85	130.00	128.88
			1645	128	2.17	125.00	4.00	130.61	131.48	130.66
			1815	175	1.00	156.60	3.27	165.54	161.84	165.58
			1820	177	1.00	156.68	3.22	166.50	162.72	166.52
			1878	183	1.00	157.43	3.21	177.00	172.78	177.05
			2013	205	1.00	158.90	2.88	198.78	195.46	198.82
			2067	199	1.00	159.30	3.17	206.45	204.21	206.48
			2074	198	1.00	159.50	3.20	207.40	205.33	207.43
			2076	201	1.00	159.51	3.12	207.67	205.65	207.71
			2136	217	1.00	159.97	2.73	215.41	215.13	215.45
			2186	222	1.00	160.38	2.63	221.35	222.85	221.39
			2304	234	1.00	161.20	2.37	233.65	240.47	233.69
2	S-H-12	S-T	1528	135	1.9	138.96	4.03	136.59	138.16	138.99
			1554	143	1.49	140.93	3.95	141.72	142.21	144.16
			1555	143	1.494	141.02	3.95	141.92	142.37	144.33
			1869	191	1.00	160.15	3.72	196.65	193.89	199.11
			1874	197	1.00	160.23	3.61	197.40	194.74	199.86
			1894	198	1.00	160.70	3.62	200.34	198.10	202.80
			2067	227	1.00	163.12	3.3	224.00	227.73	225.40
3	S-S-18	S-T	1435	103	4.522	100.91	4.83	103.91	106.27	103.31
			1468	107	4.525	111.48	4.93	113.08	114.45	113.02
			1481	117	4.22	115.57	4.77	117.00	117.71	116.93

Table 5. Comparison between the experimental measurements of Buchar et al. [2] and predicted results of both models.(Continued).

Group No.	Material designation		Impact velocity V_i [m/s]	Measured depth [2] Z [mm]	Model I		Model II			
	Rod	Target			Multiplier of Eqn. (2) c, C_t	Depth using Eqn. (2) c Z [mm]	Multiplier of Eqn. (2) c, C_t	Depth using Eqn. (2) c, Z [mm]	Depth using Eqn. (2) d, Z [mm]	Depth using Eqn. (2) e, Z [mm]
3	S-S-18	S-T	1525	127	4.03	129.21	4.79	130.12	128.80	130.06
			1845	226	1.32	215.95	4.08	214.81	210.39	214.75
			1899	229	1.26	228.52	4.20	226.75	223.81	226.69
			1975	247	1.00	237.69	4.05	242.34	242.37	242.28
			2044	241	1.00	238.72	4.43	255.30	258.84	255.24
4	S-H-18	S-T	1428	115	4.96	120.92	5.16	121.25	122.86	121.25
			1459	125	4.69	129.85	5.10	129.75	129.85	129.75
			1460	141	4.07	130.12	4.78	130.0	129.80	130.03
			1896	235	1.25	234.97	4.66	239.78	237.14	239.78
			1900	235	1.26	235.80	4.67	240.64	238.19	240.65
			1931	249	1.00	241.80	4.50	247.23	246.32	247.24
			2019	268	1.00	243.70	4.39	264.88	269.51	264.88
5	S-S-25	S-T	1423	112	5.30	105.68	5.31	108.14	111.32	108.09
			1485	118	5.47	127.59	5.60	128.63	121.02	128.58
			1527	143	4.95	141.80	5.38	142.37	140.56	142.32
			1532	145	4.92	143.52	5.38	144.00	142.00	143.95
			1999	272	2.69	271.45	5.48	273.30	273.83	273.23
6	S-H-25	S-T	1458	165	4.93	162.05	5.22	163.68	164.45	162.44
			1461	166	4.92	162.88	5.22	164.42	165.08	163.18
			1478	160	5.16	167.51	5.40	168.60	168.62	167.37
			1776	242	3.67	237.96	5.50	237.95	235.07	236.82
			1906	265	3.24	263.17	5.69	264.82	264.96	263.74
			1920	264	3.309	265.7	5.76	267.56	268.16	266.49

at each impact velocity. Table 5 also lists the values predicted and the corresponding values of the multiplier.

Figures 5 up to 8 depict the predicted penetration depth as a function of impact velocity for four rod-target interactions. Generally, it is clear from these figures that the predicted depths of penetration are in good agreement with the experimental measurements of Buchar et al. [2] over the used impact velocity range. The predicted results by Model II prove that this model has better predictive capabilities than Model I for rods having high impact velocities and aspect ratios.

For each group of data, the coefficients of the non-linear equations (2)d,e were also determined by matching the predicted depth of penetration with experimental measurements of Buchar et al. [2]. In addition, the predicted depths of penetration using these two non-linear equations are listed in Table 5.

Comparing the predicted depths of penetration using the different relations proposed, it becomes clear that the best agreement with experimental measurements is obtained when the straight line form is used. Moreover, the inclusion of rod aspect ratio in Eqn. (2)e could hardly improve the predictive capability of the model.

(ii) Samples of Predicted Results Using Model II

Figure 9 plots the time histories of the rod residual length (length of the rod rigid part) due to the impact of S-S-12 rods into S-T targets at different impact velocities. For these velocities, Model II considers the penetration process to consist of a hydrodynamic penetration phase followed by a no-penetration phase. During the first phase, the time rate at which the rod length decreases depends on the difference between the current velocity of the rod rigid part and the penetration velocity. This phase terminates when the penetration velocity vanishes. During the no-penetration phase, the remaining length of the rod rigid part is not at rest. Therefore, the time rate of change of its length depends on its current velocity.

For the same impact velocity, it is obvious from Fig. 9 that the length of the rod rigid part decreases during the penetration process. Moreover, the rod is not completely consumed during penetration. The predictions of Model II were further confirmed when compared with numerical simulation and experimental results of Holland et al. [9], who studied the penetration of stainless steel rods into steel targets. It is clear also that the rod residual length decreases with the increase of impact velocity. This is attributed to the increase of the difference between the velocity of the rod rigid part and penetration velocity during the hydrodynamic penetration phase and the increase of the velocity of the rod rigid part with impact velocity when the no-penetration phase starts. Furthermore, the model predicted the same trends for the time histories of rod residual length when the S-T targets were impacted by S-S-18 rods with different velocities.

For S-S-12 rods, the model predicts the rod residual length when the penetration process terminates and the corresponding total time of penetration at each impact velocity. For V_i = 1500, 1800 and 2200 m/s, the predicted residual lengths are 9.7, 3.23 and 0.8 mm, whereas the total times of penetration are 279, 273 and 247 μs, respectively.

Figure 10 plots the time histories of the rod residual length due to the impact of S-H-25 rods into S-T targets at different velocities. It is clear from this figure that the trend of the rod residual length is similar to that of Fig. 9, since the penetration process consists of the same phases. In addition, the model predicts the rod residual length and the total time of penetration for each interaction. For V_i = 1500, 1800 and 2200 m/s, the predicted residual lengths at the end of the penetration process are 77.9,37.7 and 12.2 mm, whereas the total times of penetration are 587, 538 and 464 μs, respectively.

For V_i = 1800 m/s, Fig. 11 plots the time histories of the rod penetration depth and its residual length due to the impact of S-S-12 and S-H-12 rods into S-T targets. It is clear from this figure that the depth of penetration increases with rod strength. This is attributed to the smaller drop in penetration velocity and the longer time of penetration taken by the rod of higher strength. In addition, it is clear from the figure that the depth of penetration of the higher strength rod slightly increases at the end of the penetration process; this increase takes place during the no-penetration phase. The model predicts the depths of penetration of S-S-12 and S-H-12 rods into S-T targets, respectively, and their total times of penetration. The predicted depth of penetration for S-S-12 rod is 162 mm and its total time of penetration is 273 μs, whereas their counterparts are respectively 186 mm and 330 μs for the S-H-12 rods.

Because the penetration velocity, U, of the S-H-12 rod is greater than that of the S-S-12 rod, the difference between the current velocity of the rod rigid part, V, and the current penetration velocity of the S-H-12 rod is less than that of the S-S-12 rod during the hydrodynamic penetration phase. Since this phase lasts much longer than the no-penetration phase, the erosion rate of the rod length during the former phase increases with the decrease of rod strength. The model predicts the residual lengths of the S-S-12 and S-H-12 rods after penetration; these are 3.23 and 29.5 mm, respectively.

Figure 12 depicts the time histories of the rod residual length and the penetration depth due to the impact of S-S-25 and S-H-25 rods into S-T targets at V_i = 2200 m/s. It is clear from this figure that the trends of the rod residual length and penetration depth, respectively, are similar to those of Fig. 11. In addition, the histories of the soft and hard rods are closer to each other than those of Fig. 11. This phenomenon has been studied numerically by Rosenberg and Dekel [10]. They attributed it to the deceleration of the rear part of the rod of high aspect ratio, which depends strongly on its strength. Therefore, the S-H-25 rod loses its velocity faster than the S-S-25 rod. They also argued that the increase of the

aspect ratio for the higher strength rod can result in a much lower penetration depth.

Figure 13 plots the predicted change of penetration depth with impact velocity for S-S-12 and S-H-12 rods, respectively. For the same impact velocity, it is clear that the depth of penetration of the hard rod is greater than that of the soft one; this is due to the increase of the penetration velocity with rod strength. For both soft and hard rods, the depth of penetration increases then decreases with the increase of impact velocity. Although the second penetration phases are not similar (no-penetration for the soft rod and rigid-rod penetration for the hard rod), the depths of penetration of both rods decrease at high impact velocities. This is attributed to the increase of the consumption rate of both rods during the hydrodynamic penetration phase at high impact velocities.

Both models predict continuously increasing depth of penetration with impact velocity. However, the experimental results of Hohler and Stilp [5] show that the depth of penetration of steel rods having aspect ratios of 10 into steel targets increases then decreases with impact velocity. Moreover, numerical simulation results of Rosenberg and Dekel [10] agree with the experimental results of Hohler and Stilp. Rosenberg and Dekel attributed this phenomenon to the high deceleration of the rigid part of the rod at high impact velocity, which reduces the rod penetration capability. Predictions of Model II are essentially similar to the experimental results of Hohler and Stilp [5].

Figure 14 plots the predicted change of penetration depth with impact velocity for S-S-25 and S-H-25 rods, respectively. It is clear that the depth of penetration increases with the increase of rod strength up to V_i = 2400 m/s. for V_i > 2400 m/s, the predicted depth of penetration of a soft rod is greater than that of a hard rod. Buchar et al. [2] show that there is no evidence of a crossover effect where a weaker rod starts to perform better than a stronger one. Their numerical simulation results predict that the value of impact velocity at which crossover occurs increases with the decrease of the rod aspect ratio. For each rod, they show that this phenomenon can lead to an optimum strength for the penetrator at which its performance will be maximum. These optimum values were determined numerically by Rosenberg and Dekel [10], but need to be confirmed experimentally.

CONCLUSIONS

Model I [1] that describes the penetration of continuous rods into thick metallic targets has been examined considering rods having aspect ratios > 10 and velocities greater than 1.5 km/s. The comparison of the predicted penetration depth with experimental measurements of Buchar et al. [2] gives poor agreement for impact velocities greater than 1600 m/s. Therefore, this model can be used to describe the penetration of a long rod (L/D ≥ 10) into a thick metallic target when the impact velocity of the rod is less than 1600 m/s.

The hydrodynamic theory developed by Tate has been modified herein by considering the essential dependence of target strength factor on the rate of deformation of its material. Three forms representing the target strength multiplier were examined. The first is a linear function of impact velocity, the second is a non-linear function of impact velocity, whereas the third is a non-linear function of impact velocity and rod aspect ratio. The predicted penetration depths are compared with the experimental measurements of Buchar et al.; good agreement is generally obtained when the linear form of the target strength multiplier is considered.

Model II covers the deficiencies of Model I. The former model is used to study the influence of rod strength on penetration depth. For rods having an aspect ratio of 12, it was found that the depth of penetration increases then decreases with impact velocity and the performance of the higher strength rod is always greater than that of the lower strength rod. For rods having an aspect ratio of 25, it was found that the performance of the lower strength rod is better than that of the higher strength rod at high impact velocity. In other words, there appears to exist an optimum rod strength for which the performance of the rod is maximum. This result is confirmed numerically and analytically by other investigators. However, it needs to be verified experimentally.

REFERENCES

1. Moustafa, K. M., Riad, A. M. and Abdel-Kader, M. S., "An Investigation of the Penetration of Semi-Infinite Metallic Targets by High-Speed Rods", Proc. 8th Int. Conf. on Applied Mechanics and Mechanical Engineering, pp. 113-130, M.T.C., Cairo, Egypt (1998).
2. Buchar, J., Lazar, M., Rolc, S., Adamik, V. and Hrebicek, J., "Long Rod Penetration Into Steel Targets", Proc. 16th Int. Symp. on Ballistics, Vol. 3, pp. 227-236, San Francisco, California, U.S.A. (1996).
3. Tate, A., "A Theory for the Deceleration of Long Rods After Impact", J. Mech. Phys. Solids, Vol. 15, pp. 387-399 (1967).
4. Tate, A., "Further Results in the Theory of Long Rod Penetration", J. Mech. Phys. Solids, Vol. 17, pp. 141-150 (1969).
5. Hohler, V. and Stilp, A. J., "Penetration of Steel and High Density Rods in Semi-Infinite Steel Targets", Proc. 3rd Int. Symp. on Ballistics, H3, Karlsruhe (1977).
6. Jones, S. E., Gillis, P. P. and Foster, JR, J. C., "On the Penetration of Semi-Infinite Targets by Long Rods", ", J. Mech. Phys. Solids, Vol. 35, pp. 121-131 (1987).
7. Wilson, L. L., Foster, JR, J. C., Jones, S. E. and Gillis, P. P., "Experimental Rod Impact Results", Int. J. Impact Engng., Vol. 8, pp. 15-25 (1989).
8. Rosenberg, Z., Marmor, E. and Mayseless, M., "On the Hydrodynamic Theory of Long-Rod Penetration", Int. J. Impact Engng., Vol. 10, pp. 483-486 (1990).

9. Holland, P. M., Gordon, J. T., Menna T. L. and Charters, A. C., "Hydrocode Results for the Penetration of Continuous, Segmented and Hybrid Rods Compared with Ballistic Experiments", Int. J. Impact Engng., Vol. 10, pp. 241-250 (1990).
10. Rosenberg, Z. and Dekel, E., "Strength Effects in Long Rod Penetration", Conf. on Structures under Shock and Impact, N. Jones, C. Brebbia and A. Watson (Eds.), Conference Series No. IV, pp. 137-148 (1995).

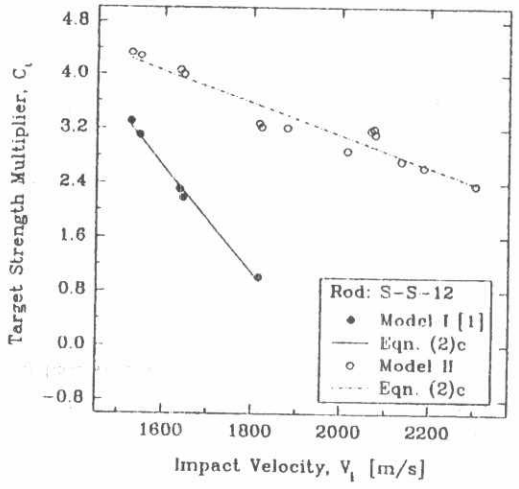

Fig. 1. Straight line fits of target strength multiplier versus impact velocity, S-S-12 rod.

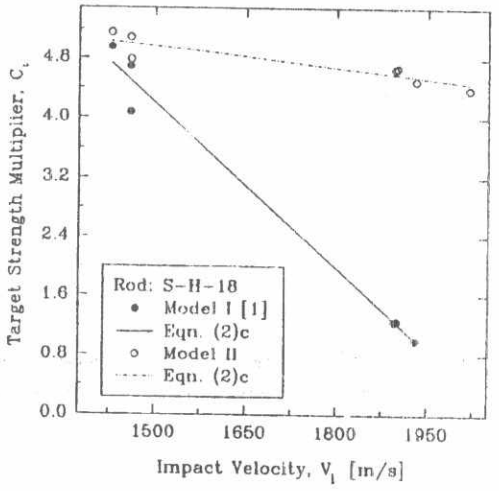

Fig. 2. Straight line fits of target strength multiplier versus impact velocity, S-H-18 rod.

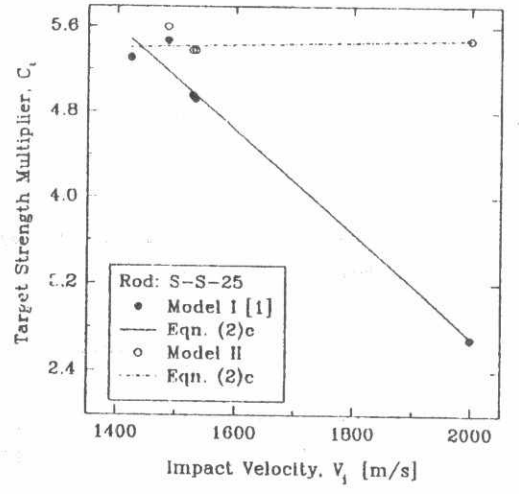

Fig. 3. Straight line fits of target strength multiplier versus impact velocity, S-S-25 rod.

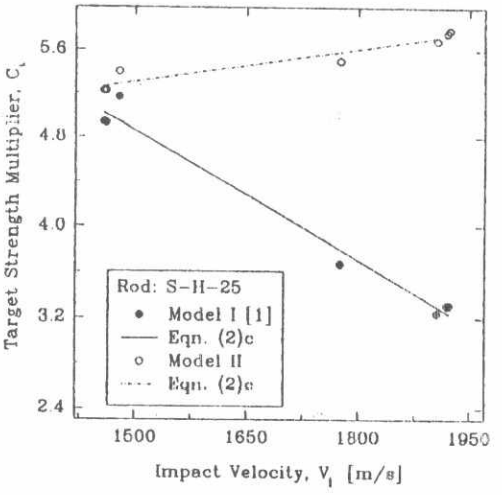

Fig. 4. Straight line fits of target strength multiplier versus impact velocity, S-H-25 rod.

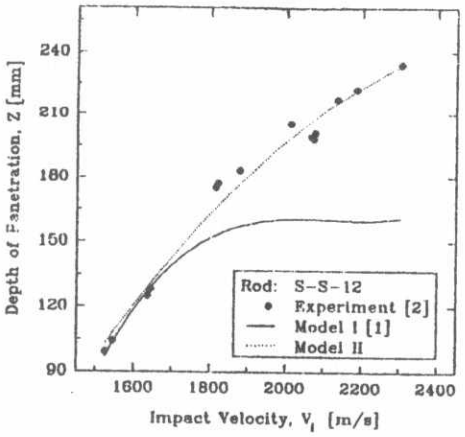

Fig. 5. Experimental [2] and predicted change of depth of penetration of Models I and II with Impact Velocity, S-S-12 rod.

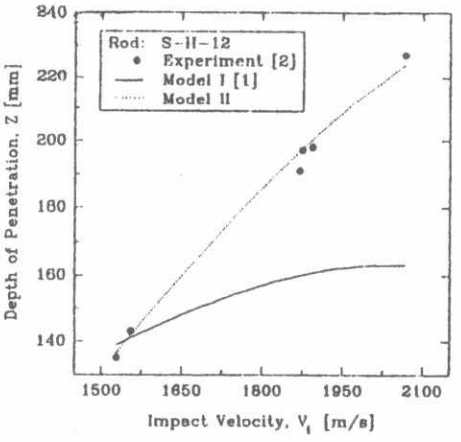

Fig. 6. Experimental [2] and predicted change of depth of penetration of Models I and II with Impact Velocity, S-H-12 rod.

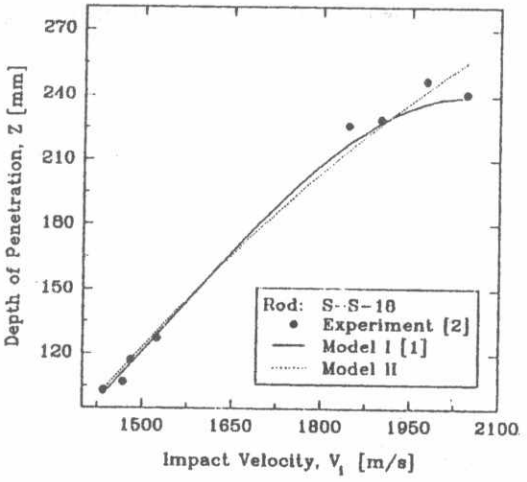

Fig. 7. Experimental [2] and predicted change of depth of penetration of Models I and II with Impact Velocity, S-S-18 rod.

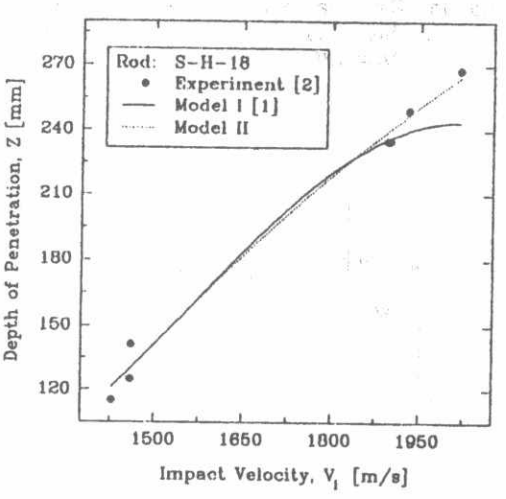

Fig. 8. Experimental [2] and predicted change of depth of penetration of Models I and II with Impact Velocity, S-H-18 rod.

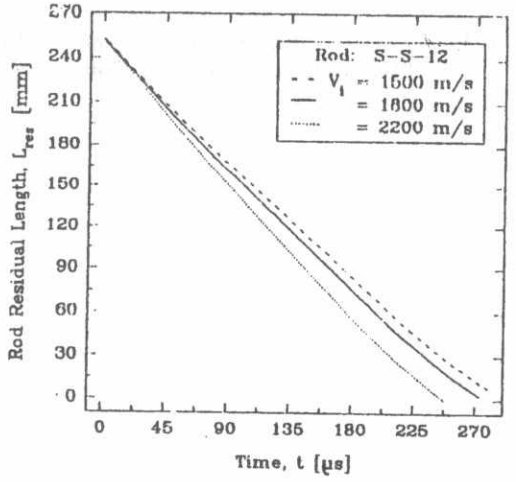

Fig. 9. Residual length-time histories, for S-S-12 rods at different impact velocities.

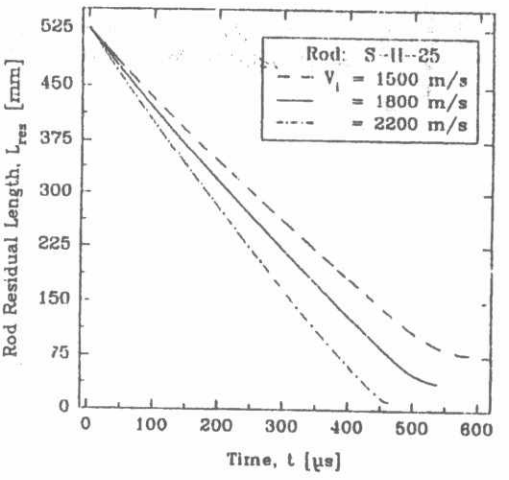

Fig. 10. Residual length-time histories, for S-H-25 rods at different impact velocities.

Proceeding of the 8th ASAT Conference, 4-6 May 1999

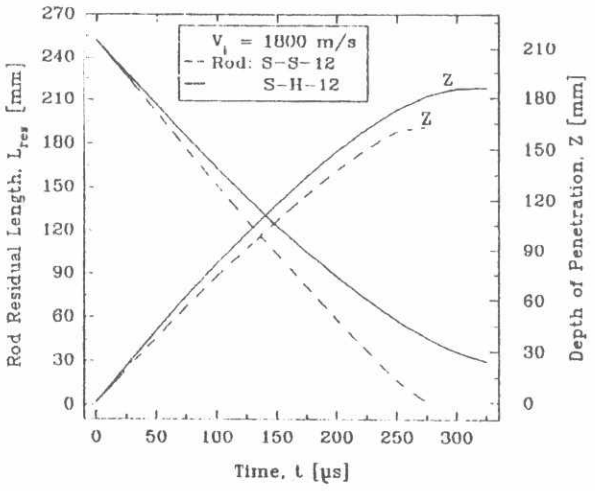

Fig. 11. Residual length and depth of penetration-time histories, for S-S-12 and S-H-12 rods at V_i = 1800 m/s.

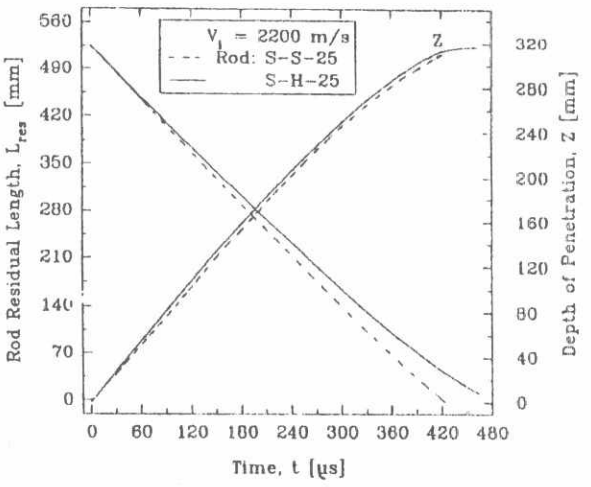

Fig. 12. Residual length and depth of penetration-time histories, for S-S-25 and S-H-25 rods at V_i = 2200 m/s.

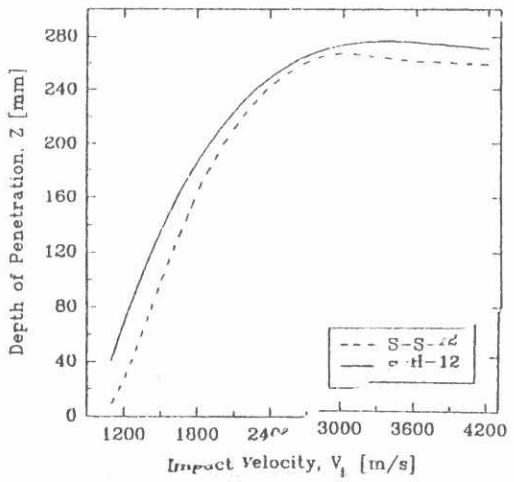

Fig. 13. Predicted change of penetration depth with impact velocity, for S-S-12 and S-H-12 rods.

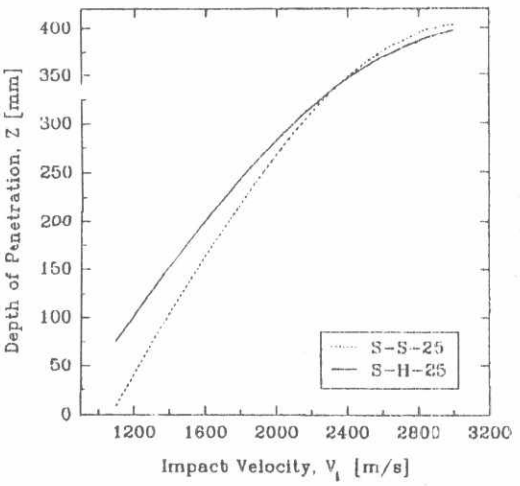

Fig. 14. Predicted change of penetration depth with impact velocity, for S-S-25 and S-H-25 rods.

Military Technical College
Kobry Elkobbah,
Cairo, Egypt

8th International Conference
on Aerospace Sciences &
Aviation Technology

On Modeling Autofrettage Residual Stresses

Y. I. El-Shaer*, M. M. Mostafa and M. S. Abdel-Kader****

ABSTRACT

In order to increase the maximum pressure a cylinder can withstand, a residual compressive stress field can be introduced near the bore. "Autofrettage" is a process used to produce such a favorable residual stress field in gun barrels.

Knowledge of residual stress distribution in Autofrettaged thick-walled tubes is a very important factor in design, fracture analysis, and fatigue life estimation. To get accurate prediction of the residual stress distribution induced by autofrettage, one should take into consideration actual material behavioral facets such as reverse plasticity and Bauschinger effect.

In this paper, Megahed and Abbas model [1] is used to predict autofrettage residual stresses. In order to successfully handle change of Bauschinger effect factor with plastic strain and non-linear hardening during reverse loading, numerical integration and equation solvers are used. Results are compared with those predicted by Chen [2] and both sets are contrasted to experimental residual stress distributions obtained by Aref, et al. [3] using electrochemical boring technique. Good agreement is generally observed between the experimental and current predicted results.

The effect of overstrain on residual hoop stress at the bore of tubes with radius ratios 2 and 3 is also studied. The results show that there is a certain overstrain value, where the stress tends to stabilize; further increase of the overstrain seems to affect the beneficial compressive stress field at the bore adversely.

KEY WORDS

Autofrettage, Residual stress, Thick-walled tubes, Reverse yielding, Bauschinger effect.

I. INTRODUCTION

Reactor pressure vessels, isostatic compaction chambers, chemical reactors, and gun barrels are only a few examples of the variety of uses of thick-walled I pressure vessels. The large tensile stress in the circumferential direction at the bore limits the maximum pressure that can be applied to the vessel.

* Assistant Lecturer, ** Assoc. Prof., Dept. Mech. Engineering, M.T.C., Cairo, Egypt.

In order to increase the maximum pressure a cylinder can withstand, a residual compressive stress fi
is a process normally used to produce such a favorable residual stress field in gun barrels.

Residual stress distribution in autofrettaged thick-walled tubes is a very important factor in design, fracture analysis, and fatigue life estimation. Therefore, this subject has met widespread interest of solid mechanics investigators such as Hill [4], Parker et al. [5], Chen [2], Bland [6], Gamer [7] and Megahed and Abbas [1].

Different assumptions used in material modeling, such as compressibility, yield criterion, flow rule, hardening rule, Bauschinger effect, etc., lead to differences between these models. To get accurate prediction of residual stress distribution induced by autofrettage, one should take into consideration actual material behavior. For instance, Megahed and Abbas [1] considered Bauschinger effect and non-linear hardening during reverse loading. However, the Baushinger effect factor was taken constant, and they handled the problem for specific values of non-linear hardening exponent during reverse loading.

The objective of the present paper is to widen the applicability and increase the accuracy of Megahed and Abbas model by taking into account the change of the Bauschinger effect factor with plastic strain and non-linear hardening during reverse loading, using numerical integration and equation solvers. Results are contrasted to experimental measurements as well as those predicted by Chen s model.

II. MATHEMATICAL MODEL

Megahed and Abbas[1] take into consideration the effect of hardening that occurs during the loading phase as well as the Bauschinger effect and the non-linear hardening during the unloading phase. They experimented with a high strength medium alloy steel characterized by linear hardening during monotonic loading and non-linear hardening during reverse loading, as may be seen from Fig.1. The monotonic curve is given by:

$$\sigma=Y+k\varepsilon_p, \qquad (1)$$

Where σ is the stress, Y is the yield stress, k is the hardening coefficient and ε_p is the plastic strain. The elastic range during unloading, shown in Fig.2 as function of plastic strain, is modeled by:

$$Y^*/Y=Q+(1-Q).\exp(-D.\varepsilon_p), \qquad (2)$$

where Y^* is half the elastic range following load reversal, D and Q, are material constants, which are determined from the reverse yielding curves of the material.

On a log-log graph, Fig.3, Eqn. (3) represents a straight line relation between ($\Delta\sigma$-$2Y^*$) and $\Delta\varepsilon_p$, that is:

$$\Delta\sigma=2Y^*+2^{1-q}.M.(\Delta\varepsilon_p)^q, \quad (3)$$

where $\Delta\sigma$ and $\Delta\varepsilon_P$ are the stress and plastic strain changes, respectively, as measured from the point of stress reversal, while M and q are material constants, which are determined from the reverse yielding curves of the material.

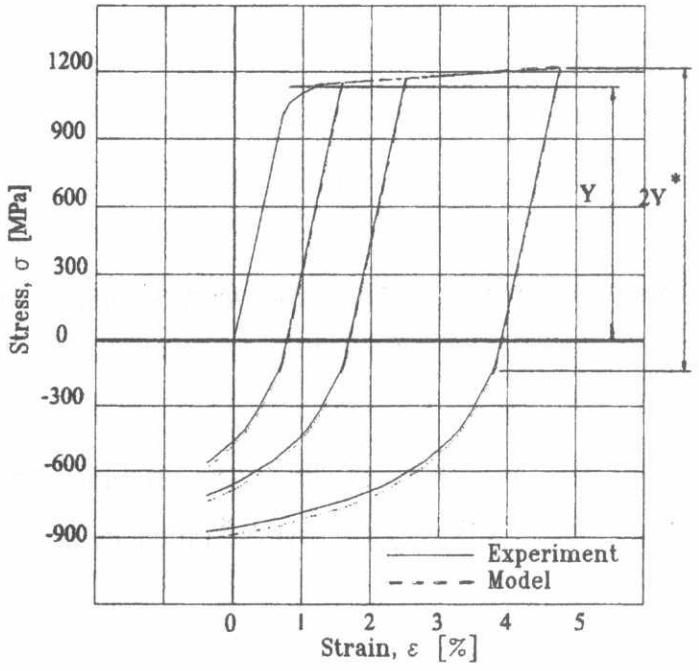

Fig.1. Comparison between model equations and experimental data for reverse loading test [1].

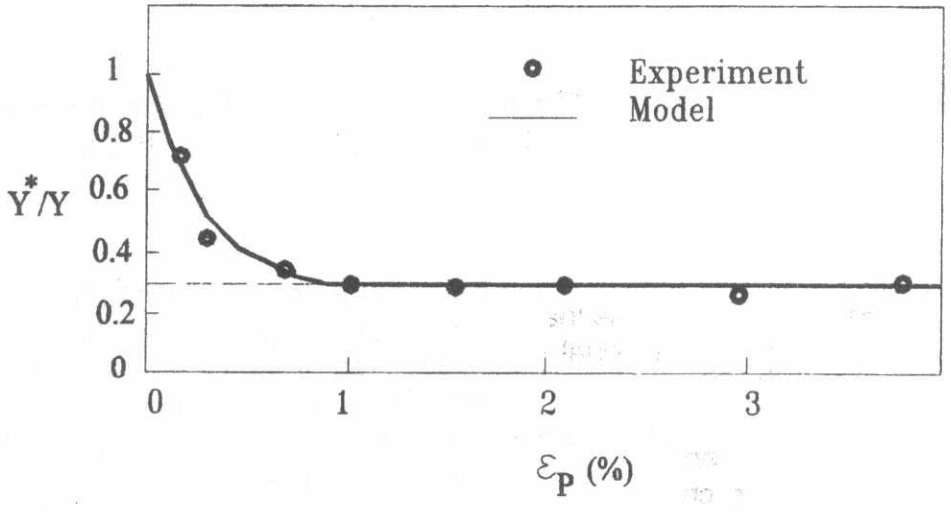

Fig.2. Variation of Y*/Y with monotonic plastic strain [1].

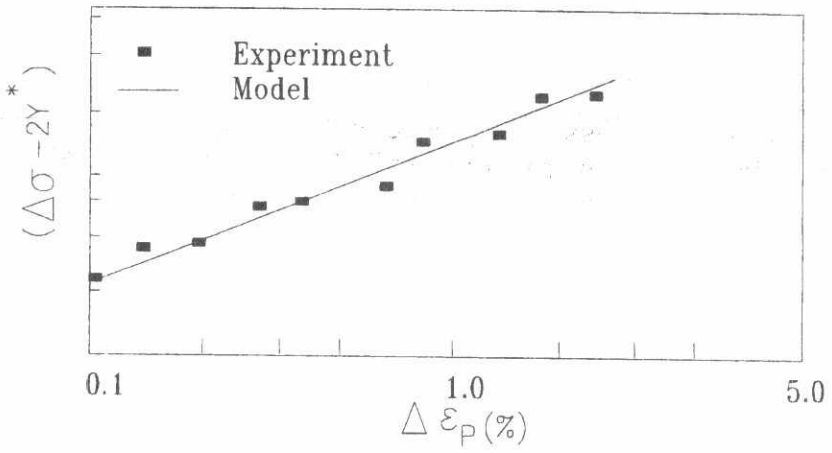

Fig.3. Representation of hardening behavior following reverse loading on a log-log plot [1].

Assuming a reverse plasticity front to occur during unloading at $X = \overline{\overline{X}}$, the distribution of the plastic hoop strain in the reverse plasticity zone, $(\Delta \hat{\varepsilon}_\theta^p)$, is given from the equation:

$$\beta\left(\Delta\hat{\varepsilon}_\theta^p\right)^q + \Delta\hat{\varepsilon}_\theta^p - \left[X/\overline{\overline{X}} - Y^*(X)/\overline{\overline{Y}}\right] = 0, \qquad (4)$$

Where $\beta = \frac{M}{\overline{\overline{Y}}}\left(\frac{\overline{\overline{Y}}}{E}\right)^q$ and $\overline{\overline{Y}} = Y^*(\overline{\overline{X}})$.

In Ref. [8], Megahed solved equation (4) for particular values of q, and due to the rapid decay of Y^* as ε_p increases, he assumed a constant Y^* value, i.e. $Y^*(X)$=Q.Y in the range of $\overline{\overline{X}} \le X \le 1$.

In order to successfully handle changes of the Bauschinger effect factor with plastic strain and non-linear hardening during reverse loading, a computer program in C++ language was constructed to calculate the residual stresses, using G-Simpson rule of numerical integration and the halfing-root method for solution of equations; the closed form solution of Megahed and Abbas derived for particular values of the material constant q was extended to encompass any arbitrary value of q, and to account for Bauschinger effect factor change with plastic strain. The procedure for calculation of residual stresses using Megahed and Abbas model is shown in Fig.4.

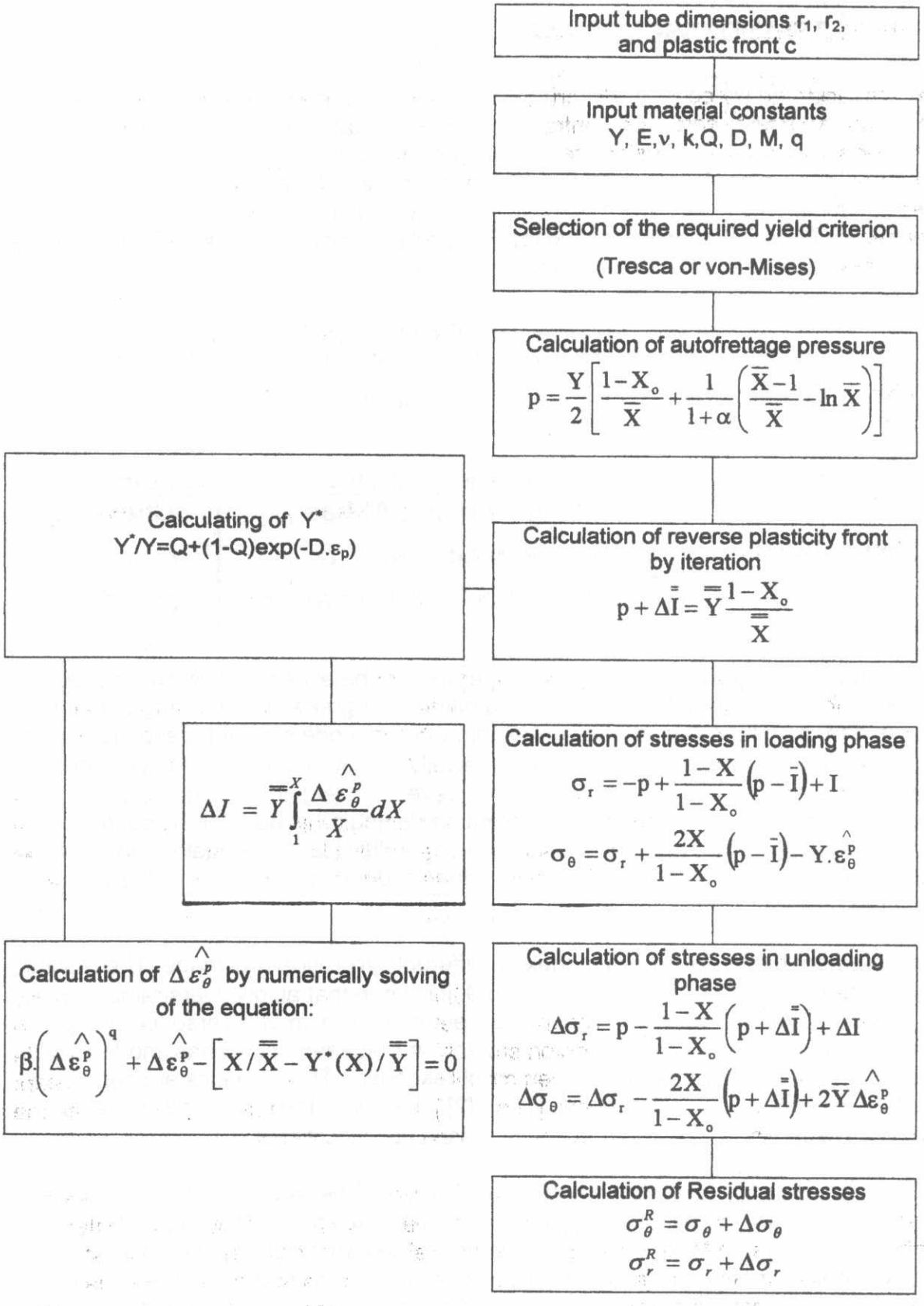

Fig.4. Procedure of calculation of residual stresses in Megahed and Abbas model.

III. RESULTS AND DISCUSSION

Results using the procedure described before are compared with those predicted by Chen [2] and both sets are contrasted to experimental residual stress distributions obtained by Aref, et al. [3] using the electrochemical boring technique.
The material chosen for investigation is medium alloy high strength steel with the chemical composition shown in Table 1. The mechanical properties and constants required for material modeling during loading and reverse loading using both models were obtained by Aref, et al.[3] and are shown in Table 2.

Table 1. Chemical composition in weight percent

C	Si	Mn	Ni	Cr	V	S	P	Fe
0.27:0.4	0.1:0.35	0.2:0.7	3.0:3.6	0.7:1.2	0.1:0.3	<0.012	<0.012	Rem.

Table 2. Mechanical properties and constants of the material used [22]

Y	E	ν	Megahed and Abbas					Chen	
[MPa]	[GPa]		K [MPa]	M [MPa]	q	Q	D	f	m̃
1080	196	0.28	2250	4730	0.43	0.61	440	0.32	0.43

The results of the two models were compared with the experimental results of Aref, et al. [3] for tubes of a radius ratio of 2 and different degrees of autofrettage in Figs.5 to 8. It can be seen from these figures that the two models provide responses that are generally close to each other specially at low overstrain Φ. Discernible differences start to appear in the zone of reverse yielding (the zone close to the bore), and can be attributed to the different hardening rules adopted by each model during unloading. Experimental results are generally closer to Megahed and Abbas model predictions, as it is closer to the actual loading and reverse loading curve of the material.

A comparison between the two models at different r_2/r_1 ratios was made. The results are plotted in Figs.9 to 11. For r_2/r_1 =2, Fig.9, it is seen that at low overstrains (Φ) the two models provide similar responses except at the region of reverse yielding. The response is seen to cross this region smoothly in Megahed and Abbas' model, while a discontinuity is observed in Chen model response. These results are consistent with those reported in references [1] and [2]. Moreover, the difference between the predicted responses of the two models increases as Φ increases

For r_2/r_1=3, Fig.10, greater differences between the two models are realized especially at high overstrains and at the zone of reverse plasticity the difference further increases. In Megahed and Abbas model the beneficial compressive stresses in the bore of the tube tend to decrease at high overstrains. The maximum compressive stress moves inwards, and an inflection point is observed at the radius ratio of 1.15 approximately for the case of Φ=100%. It means that for large radius ratios (r_2/r_1), there appears to be a limit to the beneficial compressive stresses one

can get from autofrettage. For r_2/r_1=4, a similar response to that explained before for r_2/r_1=3 is observed, as can be seen in Fig.11.

The effect of overstrain on residual hoop stress at the inner diameter of the tube was also studied on tubes of the radius ratios 2, 3 and 4. The results are shown in Fig.12. It can be seen from the figure that the residual compressive hoop stress at the bore increases with overstrain until a certain overstrain value is reached, where the stress tends to stabilize. Further increase of the overstrain seems to affect the beneficial compressive stresses in the bore adversely.

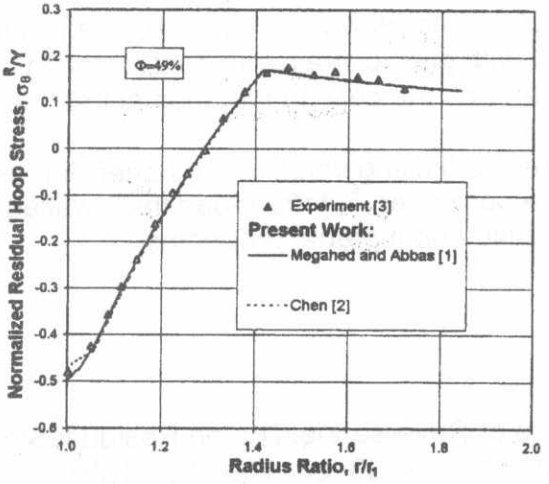

Fig.5. Experimental and predicted residual hoop stress, Φ=49 %.

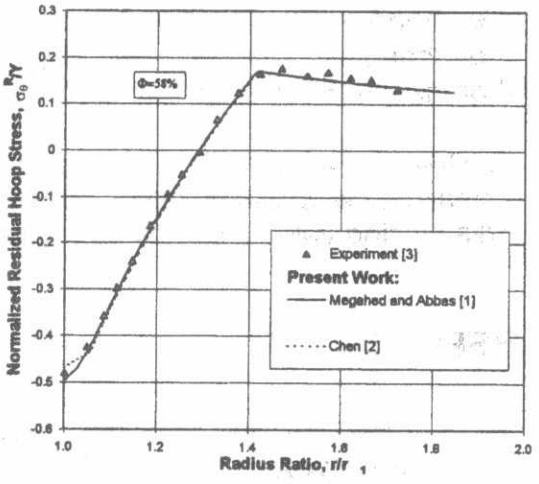

Fig.6. Experimental and predicted residual hoop stress, Φ=58 %.

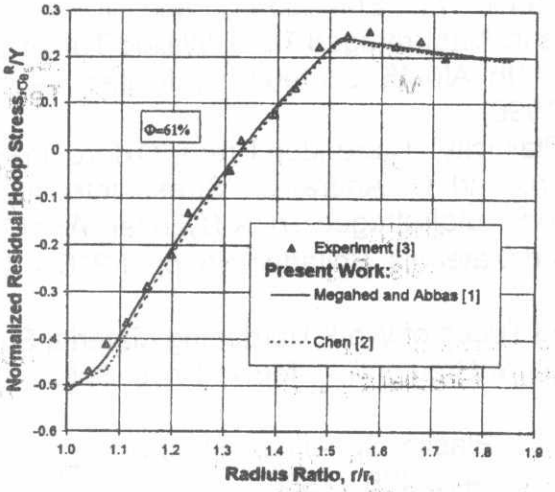

Fig.7. Experimental and predicted residual hoop stress, Φ=61 %.

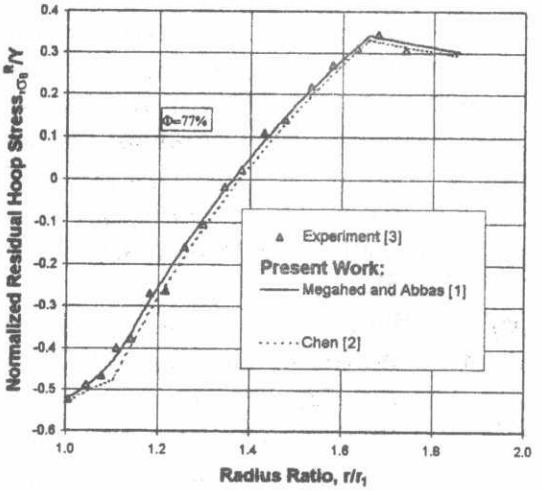

Fig.8. Experimental and predicted residual hoop stress, Φ=77 %.

CONCLUSION

Based on the results obtained from studying the residual stress distributions in autofrettaged thick-walled tubes, the following conclusions can be drawn:

a) To get accurate representation of material behavior, linear hardening during loading and Bauschinger effect factor as well as non-linear hardening during unloading should be taken into consideration.

b) In the original form of Megahed and Abbas model, equations representing reverse yielding were solved for particular values of its parameter q. In the present study, however, it was possible, using numerical integration and equations solvers, to solve the aforementioned equations for any value of q. Thus, applicability and accuracy of the model were enhanced. Accuracy of the model was further enhanced by taking the change of Bauschinger effect factor with plastic strain into consideration, rather than assuming this factor to be constant, as was the case in the original treatment.

c) Due to reverse plasticity effect, there is a limiting value to the beneficial residual compressive stresses one can get in the bore of an autofrettaged thick-walled tube. This limiting value depends on the radius ratio and material properties.

REFERENCES:

[1] M. Megahed and A. Abbas, "Influence of Reverse Yielding on Residual Stresses Induced by Autofrettage", Int. J. Mech. Sci., Vol. 33, pp. 139-150, (1991).
[2] P. Chen, "The Bauschinger and Hardening Effect on Residual Stresses in an Autofrettaged Thick-Walled Cylinder", J. of Pressure Vessel Tech., Vol. 108, pp. 108-112, (1986).
[3] N. Aref, H. Senbel, M. Abdel-Kader, M. El-Maddah, and M. Megahed, "Measurement of Residual Stresses in Autofrettaged Thick-Walled Tubes Using Electrochemical Boring Technique", 7th AMME conference, Military Technical College, Cairo-Egypt, pp. 145-155, (1996).
[4] R. Hill, "The Mathematical Theory of Plasticity", Clarendon Press, Oxford, (1950).
[5] A. Parker, J. Underwood, J. Throop, and C. Andrasic, "Stress Intensity and Fatigue Crack Growth in a Pressurized, Autofrettaged Thick Cylinder",ASTM STP 791, American Society for Testing and Materials, Philadelphia, pp. I-216 - I-237, (1983).
[6] D. Bland, "Elastoplastic Thick-Walled Tubes of Work-Hardening Material Subject to Internal Pressure and to Temperature Gradient", J. Mech. Phys. Solids Vol. 4, pp. 200-205, (1956).
[7] U. Gamer, "The Expansion of Elastic Plastic Spherical Shell with Non-Linear Hardening", Int. J. Mech. Sc., Vol. 30, pp. 415-426, (1988).
[8] M. Megahed, "Elasto-Plastic Behavior of Thick-Walled Tube with General Nonlinear Hardening Properties", Int. J. Mech. Sci., Vol. 32,pp. 551-563, (1990).

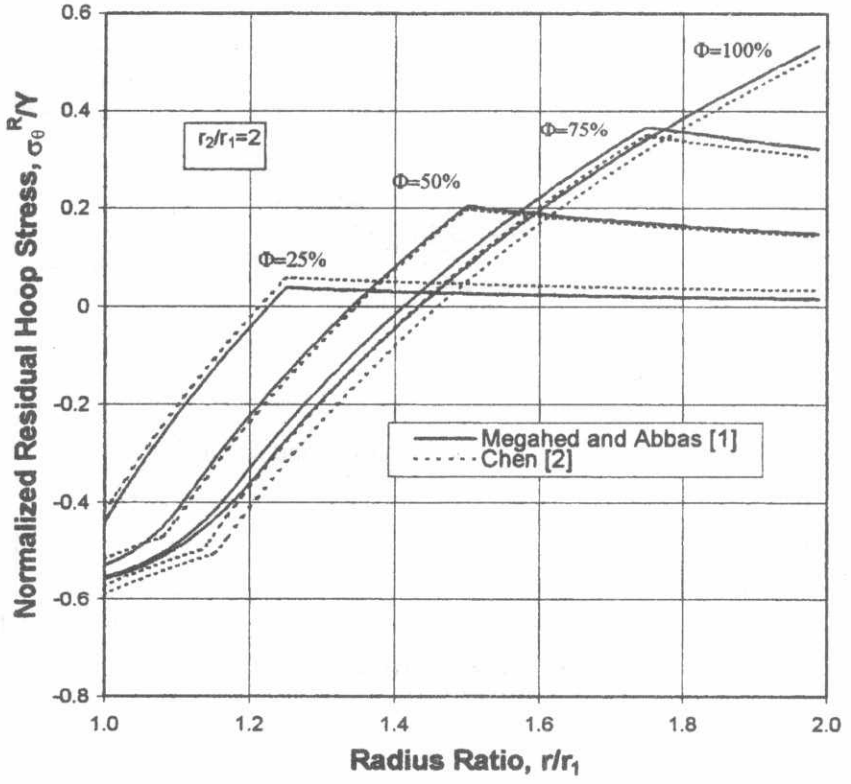

Fig.9. Residual hoop stress at different overstrains, $(r_2/r_1)=2$.

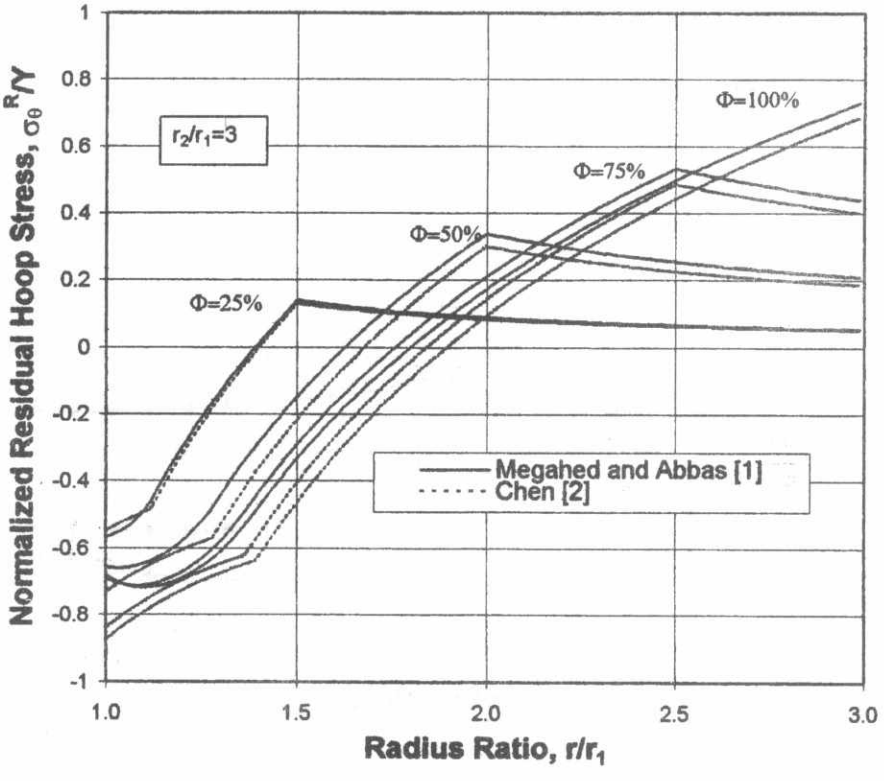

Fig.10. Residual hoop stress at different overstrains, $(r_2/r_1)=3$.

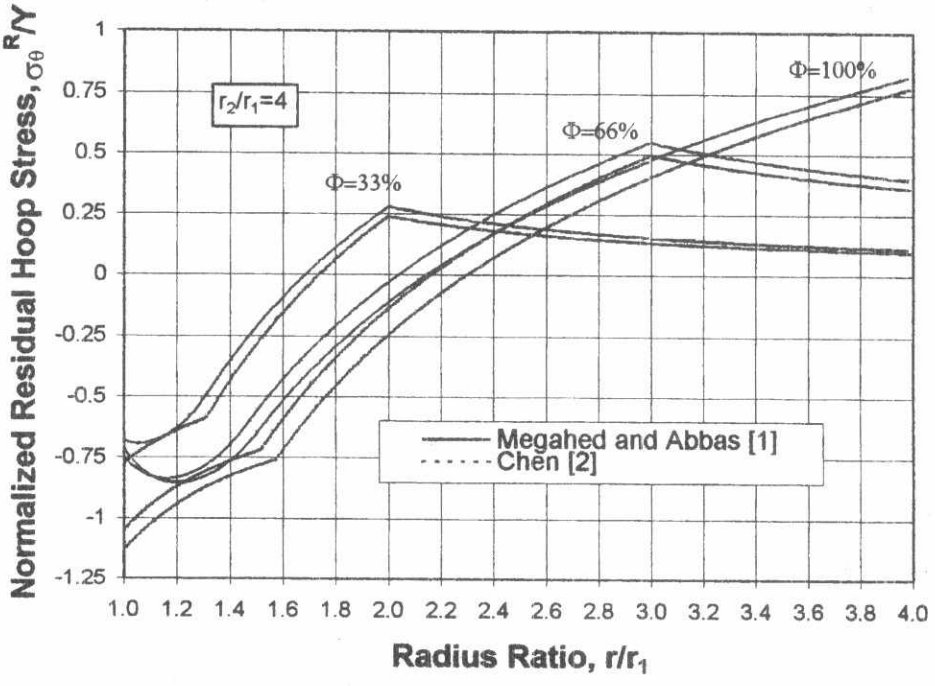

Fig.11. Residual hoop stress at different overstrains, $(r_2/r_1)=4$.

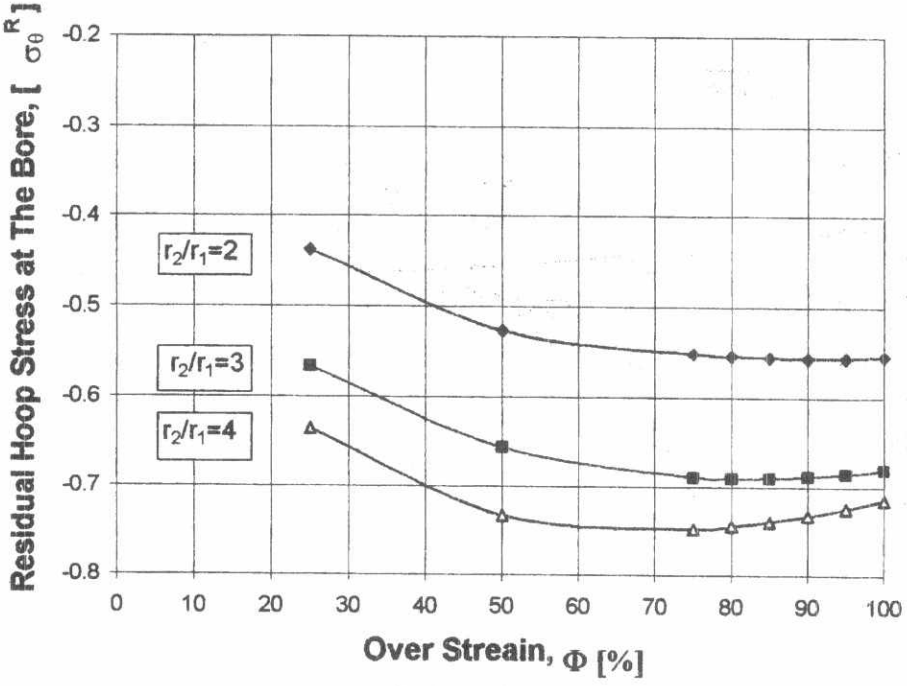

Fig.12. Effect of overstrain on residual hoop stress at the bore.